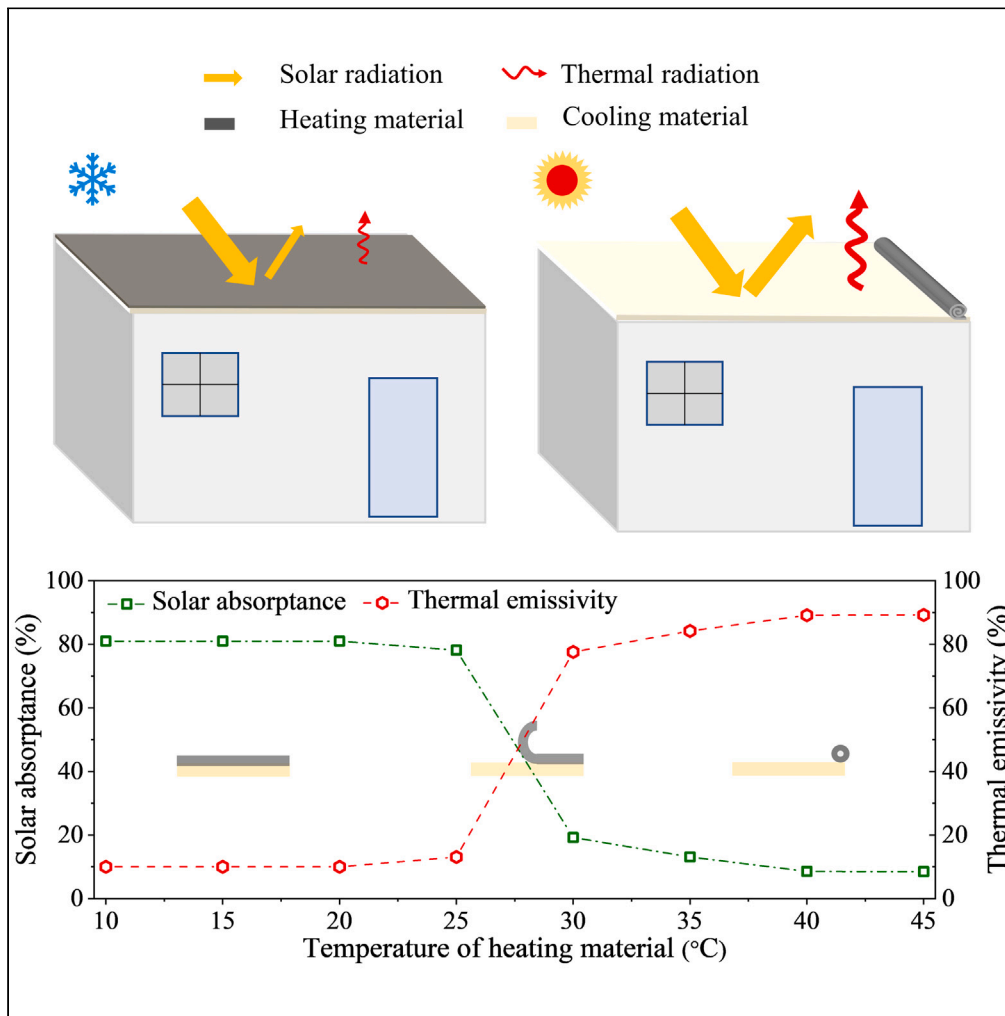


Article

# Temperature-adaptive rooftop covering with synergetic modulation of solar and thermal radiation for maximal energy saving



Jiale Chai,  
Jianheng Chen,  
Zhanxiao Kang,  
Lin Lu, Chi-Hung  
Tang, Jintu Fan

[jintu.fan@polyu.edu.hk](mailto:jintu.fan@polyu.edu.hk)

**Highlights**

Synchronous solar and thermal radiation modulations are achieved for building rooftop

The proposed device is fabricated in easy-to-be-implemented process

The proposed device can achieve all-season energy savings in all climate regions

The proposed concept is also applicable to other radiation-regulated fields

Chai et al., iScience 26, 107388  
August 18, 2023 © 2023 The Authors.  
<https://doi.org/10.1016/j.isci.2023.107388>



## Article

## Temperature-adaptive rooftop covering with synergetic modulation of solar and thermal radiation for maximal energy saving

Jiale Chai,<sup>1</sup> Jianheng Chen,<sup>2</sup> Zhanxiao Kang,<sup>1</sup> Lin Lu,<sup>2</sup> Chi-Hung Tang,<sup>3</sup> and Jintu Fan<sup>1,4,\*</sup>

## SUMMARY

The energy consumption for maintaining desired indoor temperature accounts for 20% of primary energy use worldwide. Passive rooftop modulation of solar/thermal radiation without external energy input has a great potential in building energy saving. However, existing passive rooftop modulation techniques failed to simultaneously modulate solar/thermal radiation in response to rooftop surface temperature which is closely related to the building thermal loads, leading to limited or even counter-productive overall energy saving. Here, we report the development of a surface temperature-adaptive rooftop covering with synergetic solar and thermal modulations. The covering, made of a scalable metalized polyethylene film, demonstrated excellent solar absorptance modulation (72.5%) and thermal emissivity modulation (79%) in response to its temperature change from 22°C (indoor heating setpoint) to 25°C (indoor cooling setpoint), and vice versa. Building energy simulations demonstrate that the proposed rooftop covering can achieve all-season energy savings across all climate regions.

## INTRODUCTION

The building sector accounts for 40% of primary energy use worldwide,<sup>1</sup> of which 50% is consumed to maintain desired indoor temperature by removing building thermal loads.<sup>2</sup> Regulation of solar and thermal radiation of building rooftop shows great promise to reduce building thermal loads for energy savings.<sup>3–5</sup> In principle, to maximize the energy savings, the rooftop should achieve high solar absorptance but low thermal emissivity in cold seasons to increase the rooftop surface temperature for reducing building heat loss (i.e., heating loads), while it should achieve low solar absorptance but high thermal emissivity in hot seasons to decrease rooftop surface temperature for reducing building heat gain (i.e., cooling loads) (Figures 1A and 1B). Unfortunately, the prevailing radiation-regulation rooftop materials show fixed solar absorptance and thermal emissivity,<sup>6–9</sup> and they can only help decrease the building cooling loads in summer but inevitably increase the heating loads in winter. Consequently, the reduced cooling energy use may be counteracted or even surpassed by the increased heating energy use, especially in heating-dominated regions. To overcome such limitations, a few attempts have been devoted to modulating the optical properties of the rooftop materials, which may accommodate the actual heating/cooling needs of building in different seasons (Table S1). Among them, the most effective strategy is to simultaneously modulate solar absorptance and thermal emissivity of the rooftop materials. Nevertheless, such synergetic modulation is mainly activated by electricity or mechanical force.<sup>10–15</sup> Although these materials show potentials to decrease building energy needs all year round, they usually require external power inputs and involve sophisticated manufacturing process.

Compared with the electrical-/mechanical-driven types, the temperature-adaptive rooftop materials/devices are more promising in practice since they require no external power inputs. Broadly speaking, the existing works can be classified into two groups. In the first group, the temperature-adaptive materials/devices can only achieve either solar or thermal modulations, not both. The solar modulation was achieved by mixing the thermochromic paints (Leuco dyes) with titanium oxide particles, which could switch the solar absorptance accompanying with color change in response to surface temperature variations.<sup>16–22</sup> Nevertheless, their thermal emissivity is constant and usually exceeds 90%, which would accelerate the building heat loss in cold seasons, resulting in increased building heating loads. The thermal modulation was carried out by using vanadium dioxide (VO<sub>2</sub>)-based Fabry-Perot (FP) resonator, which switched its thermal emissivity through the temperature-induced phase change of VO<sub>2</sub> and the FP resonance.<sup>23–29</sup> Whereas, the

<sup>1</sup>School of Fashion and Textiles, The Hong Kong Polytechnic University, Kowloon, Hong Kong, China

<sup>2</sup>Renewable Energy Research Group (RERG), Department of Building Environment and Energy Engineering, The Hong Kong Polytechnic University, Kowloon, Hong Kong, China

<sup>3</sup>The Surface Engineering Unit of the Additive Manufacturing Stream, Industrial Centre, the Hong Kong Polytechnic University, Kowloon, Hong Kong, China

<sup>4</sup>Lead contact

\*Correspondence: jin-tu.fan@polyu.edu.hk  
<https://doi.org/10.1016/j.isci.2023.107388>



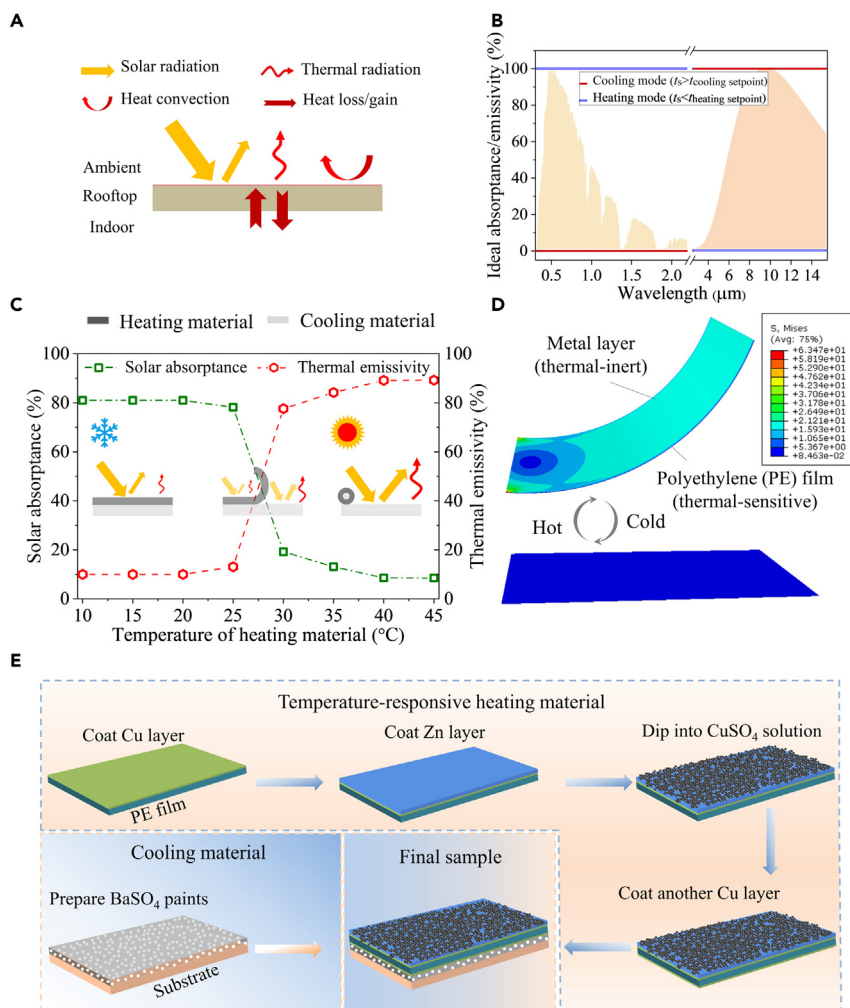


**Figure 1. Proposed temperature-adaptive rooftop covering with synergetic radiation modulations and its fabrication process**

(A) Schematic of heat transfer of building rooftop.

(B) Ideal absorptance/emissivity of building rooftop within the solar and infrared spectrum (the light yellow and orange shadows represent the normalized spectra of AM1.5 solar radiation and blackbody radiation at 300 K, respectively).  $t_s$  is rooftop surface temperature, while  $t_{\text{heating/cooling setpoint}}$  is the indoor heating/cooling setpoint ( $22^{\circ}\text{C}/25^{\circ}\text{C}$  in the study), respectively).

(C) Schematic of the proposed rooftop covering for synergetic solar and thermal modulations, and the associated temperature-adaptive optical properties.

(D) Bending actuation of a metalized polyethylene (PE) film in response to temperature change simulated using ABAQUS software.

(E) Fabrication process of the proposed rooftop covering (one ends of the heating and cooling materials are bonded together in the final sample).

resonator usually shows constant solar absorptance, which cannot effectively regulate the solar heat in different seasons, resulting in limited or even counter-productive overall energy savings. Besides, there are other temperature-responsive materials with thermal emissivity modulation, i.e., chalcogenide<sup>30–33</sup> and perovskite oxide.<sup>34–38</sup> Nevertheless, the former requires much higher transitional temperature (usually above  $150^{\circ}\text{C}$ ) while the latter experiences wider transition temperature range (e.g., from  $-176^{\circ}\text{C}$  to  $100^{\circ}\text{C}$ ), hindering their application on buildings.

In the second group, the temperature-adaptive materials/devices could achieve both solar and thermal modulations. To the best of our knowledge, there are only three studies on the temperature-induced synergetic

modulations.<sup>39–41</sup> One was a theoretical work using rigorous nanophotonic structures with ideal assumption,<sup>39</sup> while the other two<sup>40,41</sup> were from the same group, reporting synergetic modulations using a temperature-responsive polymer. The former<sup>40</sup> indeed achieved the two modulations separately rather than synchronously (solar modulation was achieved between 30°C and 35°C while thermal modulation was achieved between 40°C and 55°C). The separate modulations may fail to accommodate the actual building heating/cooling needs in practice, resulting in limited or even deteriorated energy savings. Although the latter<sup>41</sup> can achieve synchronous modulation, both solar absorptance and thermal emissivity changed very slowly as temperature decreased at heating mode, resulting in much limited heating performance. Besides, they both required sophisticated fabrication process, which hindered their practical application. Until now, developing energy-efficient temperature-adaptive rooftop material/device still poses significant challenge.

Here, we developed a temperature-adaptive rooftop covering with synergetic modulation of solar and thermal radiation for maximum energy savings. In this work, the temperature-adaptive material/device was activated by its own temperature rather than the ambient temperature. The synergetic modulation was achieved synchronously, and both solar absorptance and thermal emissivity can change quickly as temperature changed at both cooling and heating modes. Besides, the proposed roof covering was fabricated in simple process. The covering was composed of a bilayer structure having a temperature-responsive heating material at the top and a cooling material at the bottom. It demonstrated excellent solar absorptance modulation (72.5%) and thermal emissivity modulation (79%) in response to the temperature change of the top heating material. In the cold ambient, the covering was in the solar heating mode and exhibited high solar absorptance (81%) but low thermal emissivity (10%) to suppress the building heat loss. In the hot ambient, the covering was in the radiative cooling mode and exhibited low solar absorptance (8.5%) but high thermal emissivity (89%) to reduce the building heat gain. Experiments demonstrated the effectiveness of the proposed rooftop covering in regulating roof surface temperature in cold and hot weather conditions. Building energy simulation further demonstrated that the proposed covering can achieve year-round building energy savings in all climate regions in comparison with conventional heating and cooling roof materials. This work opens pathway to achieve synergetic modulation of solar and thermal radiation of rooftop for maximum energy savings. We foresee that this concept can also be applied to other fields where radiation modulation is required under different temperatures, such as outdoor personal thermal management,<sup>42,43</sup> solar heat storage system.<sup>44,45</sup>

## RESULTS

### Working principle and fabrication process

The proposed rooftop covering consists of two layers, and one ends of them are bonded together. The upper layer is a temperature-responsive heating material with high solar absorptance but low thermal emissivity, while the lower layer is a cooling material with low solar absorptance but high thermal emissivity. The synergetic modulation of solar and thermal radiation is attributed to the thermal-induced bending actuation of the heating material, which is made of a metalized polyethylene (PE) film. In comparison with other polymers, the PE film has a relatively high thermal expansion coefficient ( $\sim 100 \times 10^{-6}/\text{K}$ ) due to the simple and long C-C chemical bonds along its main chain.<sup>46</sup> To fully utilize this thermal-responsive property for thermal regulation, a metal layer with much lower thermal expansion coefficient ( $\sim 10 \times 10^{-6}/\text{K}$ ) is coated onto it to form a temperature-responsive actuator. When temperature increases, the PE film expands due to its much higher expansion ratio, while the metal layer largely retains its dimension as its expansion ratio is one magnitude smaller. As the two layers are bonded together, the actuator bends up due to the large mismatch of the two expansion ratios. When temperature decreases, the PE film would contract and the stress within the actuator will release. Consequently, the actuator recovers back to the original flat shape. The finite element simulation using ABAQUS software confirms the bending actuation of the actuator in response to temperature changes (Figure 1D). The parameters of each substance used in ABAQUS software (e.g., Young's modulus and Poisson's ratio) are obtained from ref.<sup>47–49</sup>.

Owing to such temperature-induced bending actuation, the rooftop covering achieves synergetic radiation modulations and thus it can accommodate the building heating/cooling needs in different seasons. In the cold season, the heating material keeps flat, and it largely absorbs solar heat and simultaneously suppresses the building heat loss owing to its low thermal emissivity, thereby increasing the roof's surface temperature and reducing building heating needs. As temperature increases, the heating material would gradually bend up. Correspondingly, the solar absorptance of the rooftop covering would decrease while the thermal emissivity would increase. In the hot season, the heating material would further form small rolls,

and the cooling material is fully exposed to the ambient. In this state, most of the solar radiation would be reflected and the building heat would largely dissipate into ambient due to its high thermal emissivity, thereby decreasing the roof's surface temperature and reducing building cooling needs. Mentioned that in practice, the temperature of heating material is jointly determined by the ambient temperature and solar heat, and thus affects the associated bending properties (Video S1).

The fabrication process of the proposed rooftop covering is illustrated as follows (Figure 1E). We have tried the widely used metal coating methods (including the electroless plating and electroplating) to coat the Cu layer onto PE films, which were cheap and fast techniques.<sup>50,51</sup> For the electroless plating, we found that as the surface of the PE film was too smooth, the catalysis cannot adhere onto it, leading to unsuccessful coating. For electroplating, we found that as the PE film was not electroconductive, the Cu layer cannot be directly coated on it. To the best of our knowledge, the magnetron sputtering was the most appropriate technique to coat the Cu layer onto the PE film. For the heating material fabrication, a very thin layer (~5 nm) of copper was firstly deposited onto a PE film using magnetron sputtering, and then a thick layer (~1000 nm) of zinc was electrodeposited onto the electroconductive film. Here, the thick zinc layer was not directly deposited onto the PE film using sputtering as it would cause severe thermal stress within the PE film and result in curly shape (Figure S1). The metalized film was further dipped into a copper sulfate (CuSO<sub>4</sub>) solution, washed using deionized water, and dried. The dipping process resulted in Cu nanoclusters on the zinc layer with plasmonic resonance that induced strong solar absorption.<sup>13,52</sup> The fabrication process also led to low thermal emissivity due to the metallic components. Note that as the Cu nanoclusters randomly dispersed onto the Zn layer rather than forming dense metal layer, they had little impacts on the bending properties of the heating material. Lastly, a very thin layer of copper was coated onto the other side of the PE film. This step can slightly increase the temperature at which the heating material began to bend from 22°C to 25°C (Figure S2), which was an energy-efficient indoor cooling setpoint recommended by Department of Energy of U.S.<sup>53</sup> Regarding the cooling material fabrication, there were several choices (e.g., randomized glass-polymer hybrid metamaterial,<sup>7</sup> cellulose nanofiber-based wood,<sup>8</sup> and barium sulfate - BaSO<sub>4</sub> paint<sup>54</sup>). In this work the BaSO<sub>4</sub> paint was selected since it showed excellent optical properties but with easy-to-be-implemented fabrication process. The BaSO<sub>4</sub> powders were directly mixed with the acrylic resin and ultrasonicated for 30 min. Then, the mixture was coated onto a substrate (white hardboard), and dried for 24 h. At last, the heating material was placed onto the cooling material, and one ends of them were bonded together.

### Optical and bending properties

The temperature-adaptive optical properties of the proposed rooftop covering (Figure 1C) were jointly determined by the tailored optical properties of the heating and cooling materials, and the tailored temperature-responsive bending properties of the heating material. For the heating material, the optical properties were tailored by changing the dipping time. As the dipping time increased from 20 to 30 s–40 s to 50 s and 60 s, the solar absorptance increased from 50.8% to 71.9%–81.0% to 82.8% and 85.1% while the thermal emissivity increased from 7.6% to 8.4%–10.3% to 14.8% and 16.2% (Figure S3), respectively. To identify the optimal solar absorptance and thermal emissivity, we assumed the heating material to achieve thermal equilibrium under solar absorption and sky radiative cooling, and quantified the associated surface temperature (Figure S4). The results showed that the heating material achieved the highest surface temperature under the dipping time of 40 s, indicating the best heating performance. Thus, the optimal solar absorptance and thermal emissivity of the heating material was identified as 81% and 10.3%, respectively. For the cooling material, the optical properties were tailored by varying the volume fractions of the BaSO<sub>4</sub> particles. As the volume fraction increased from 2% to 4%–6% to 8% and 10%, the solar absorptance decreased from 16.3% to 8.6%–5.3% to 4.7% and 4.3% while the thermal emissivity decreased from 93.6% to 93.3%–93.2% to 92.7% and 92.4% (Figure S5). It showed that both solar absorptance and thermal emissivity decreased little as the fraction increased from 6% to 10%. To further evaluate the cooling effects of the material under different sets of optical properties, the associated surface temperature was quantified at thermal equilibrium state considering both solar absorption and sky radiative cooling. With the increase of the volume fraction (Figure S6), the surface temperature sharply decreased in the beginning (from 2% to 6%) and then stabilized afterward (from 6% to 10%). In other words, the cooling effects increased little as the fraction was larger than 6%. Taking the initial cost into consideration, we finally identified the optical properties at the volume fraction of 6% as the optimal ones. In brief, the heating and cooling materials (Figure 2A) achieved tailored solar absorptance of 81.0% and 5.3%, respectively, while achieved tailored thermal emissivity of 10.3% and 93.2%, respectively (Figure 2B).

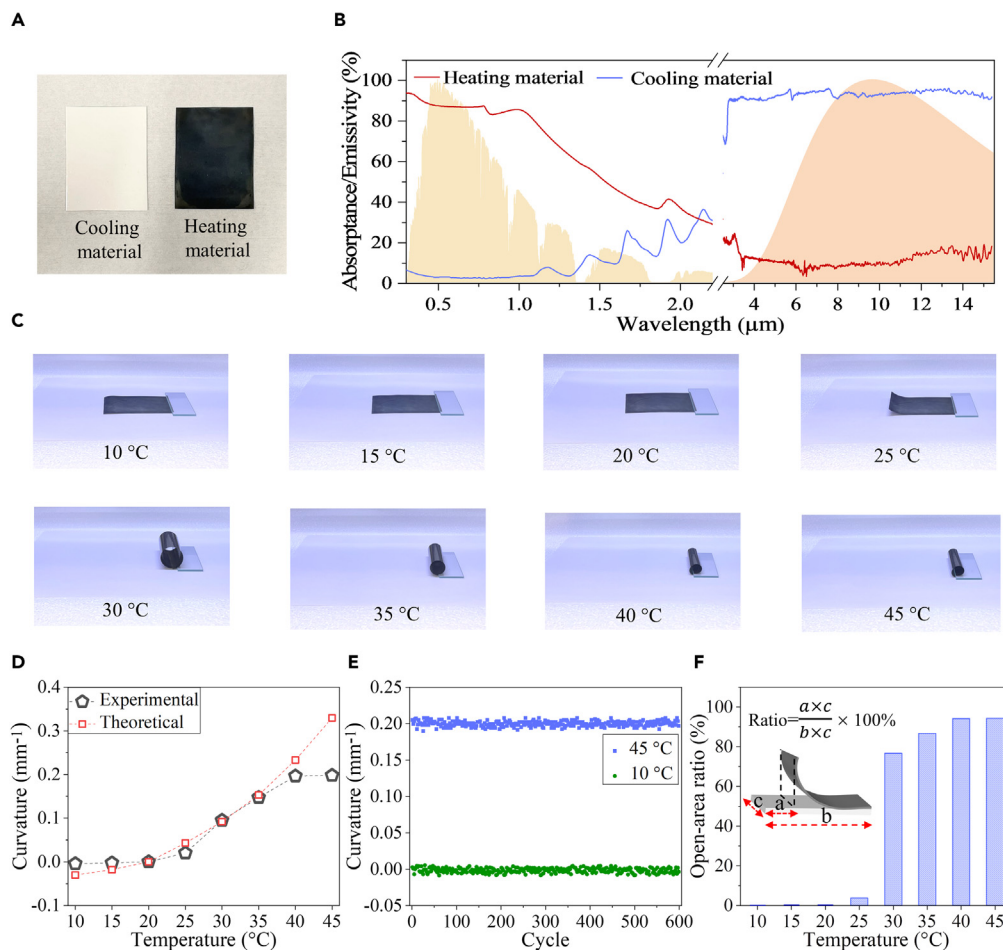


**Figure 2. Optical and bending properties of the heating and cooling materials**

- (A) Optical images of the cooling and heating materials.  
 (B) Tailored solar absorbance and thermal emissivity of the cooling and heating materials.  
 (C) Optical images of the tailored heating material in the temperature range of 10°C–45°C.  
 (D) Bending curvature comparisons between the experimental and theoretical results.  
 (E) Bending curvatures of the tailored heating material at 10°C and 45°C within 600 cycles.  
 (F) Open-area ratio of the rooftop covering at different temperatures.

The impacts of the dipping time and thickness of each layer on the response time and modulation effect were investigated. As the modulation effect was jointly determined by the bending property and optical property of the material, the bending property was also presented. Figure S7A showed that the dipping time had little impacts on the response time and bending properties (i.e., bending curvature). As the dipping time increased from 20 to 60 s, the solar absorbance modulation increased from 50.5% to 76.2% while thermal emissivity modulation decreased from 81.6% to 72.2% (Figure S7B). As discussed earlier, the optical properties under dipping time of 40 s were chosen at last since they resulted in the best heating performance (Figure S4). Figure S8A showed that the PE film thickness had large impacts on the response time and bending properties. As the PE film thickness increased, the response time increased while the bending property decreased, which further resulted in deteriorated solar absorbance and thermal emissivity modulations (Figure S8B). The PE film thickness of 40  $\mu\text{m}$  was chosen at last as it led to the highest modulation properties. Mentioned that a thinner PE film (e.g., 30  $\mu\text{m}$ ) was not considered since it would bend up even at heating mode and thus it would accelerate the building heat loss, leading to deteriorated building energy savings. Figure S9A showed that the metal layer thickness had little impacts on the response time while had large impacts on the bending property. The thickness of 1000 nm was chosen at last since it resulted in the highest modulation properties (Figure S9B). The tailored sample was almost flat as temperature was lower than 25°C, while it bended up and finally formed small rolls with the further increase of temperature

(Figure 2C). The bending curvature measured from the optical images kept almost zero at low temperature (10°C, 15°C, and 20°C), while it sharply increased and then gradually stabilized as temperature increased from 25°C to 45°C. The response time of the proposed rooftop covering was 10 s when temperature increased from 25°C to 45°C, while the associated recovery time was 40 s as temperature decreased from 45°C to 25°C. The measured curvatures agreed well with the theoretical results derived from Hooke's law (Figures 2D and S16). The slight discrepancy may be attributed to the deviations of physical parameters (e.g., layer thickness, Young's modulus), supporting force from the ground, neglected effect of shear force, etc.<sup>55,56</sup> For instance, at lower temperature (e.g., 10°C), the supporting force from the ground can offset the bending force of the film toward the ground so that the film can still keep flat. The bending stability of the sample was another important factor in application. The sample showed highly repeatable changes of bending curvature as the temperature varied from 10°C to 45°C within 600 cycles (Figure 2E), indicating high stability. Last, the open-area ratio was quantified, which was defined as the area percentage of the cooling material covered by the heating material (see the inserted schematic in Figure 2F). A larger ratio indicated more solar would be reflected and more infrared thermal would dissipate into the ambient, and vice versa. The ratio was measured from the optical images, and it was highly correlated with the bending property of the heating material (Figure 2F). Based on the tailored optical properties and the open-area ratio, the solar absorptance and thermal emissivity of the rooftop were quantified (Figures S17 and S18), and the associated results will be adopted in the building energy simulation.

### Roof surface temperature test

The temperature-adaptive synergetic solar and thermal modulations of the proposed rooftop covering lay the foundation of effective regulations of roof surface temperature in different seasons. We demonstrated its temperature regulation capabilities by monitoring the temperatures of three samples (i.e., proposed rooftop covering, conventional cooling and heating roof materials with the same dimensions of 7.5 cm × 5.5 cm) under cold and hot ambient conditions, respectively. The stabilized roof surface temperature was jointly determined by the solar absorptance and thermal emissivity of different materials/devices. The solar absorptance and thermal emissivity of the conventional cooling roof material were 13.6% and 92.1%, respectively, while those of the conventional heating roof material were 83.7% and 93.8%, respectively (Figure S10). The conventional heating and cooling roof materials were copper oxide (CuO)-based and titanium dioxide (TiO<sub>2</sub>)-based roof coatings, respectively, which were widely used in existing studies.<sup>57–59</sup> The experimental setup was shown in Figure 3A. We controlled the ambient temperature and adopted solar simulator to simulate the weather conditions in cold and hot seasons. The temperature was recorded using a data record system. To improve the measurement accuracy, two thermocouples were installed onto each sample and their average value was considered as the roof surface temperature. The solar simulator in our lab can only simulate the solar intensity between 80 and 560 W/m<sup>2</sup>, while the ambient temperature of our lab can only be controlled between 8°C and 26°C. For simplicity, this work adopted 80 W/m<sup>2</sup> and 8°C to simulate the cold weather, while adopted 560 W/m<sup>2</sup> and 26°C to simulate the hot weather.

Under cold weather condition, when the simulator was on, the temperatures of the three samples sharply increased in the beginning and stabilized afterward. The proposed rooftop covering and conventional cooling material showed the highest (17.1°C) and lowest (11.3°C) stabilized temperatures, respectively (Figure 3B). The reason was explained as follows. Although the solar absorptance of the proposed covering (81%) was a little smaller than that of the conventional heating material (83.7%), the thermal emissivity of the former (10.3%) was much smaller than that of the latter (93.8%), indicating excellent thermal insulation capability. As a result, the temperature of the proposed covering was higher than that of the conventional heating material. Since the conventional cooling material showed much smaller solar absorptance and poor thermal insulation capability, it achieved the lowest stabilized temperature. Under hot weather condition, when the simulator was on, the temperatures of the three samples also sharply increased in the beginning and stabilized afterward. The proposed covering and the conventional heating material showed the lowest (38.4°C) and highest (56°C) stabilized temperatures, respectively (Figure 3C). For the proposed rooftop covering, the conventional heating material in the upper layer largely absorbed the strong solar light and form small rolls once the simulator was on, which made the cooling material in the lower layer fully exposed to the solar light. The smaller solar absorptance of the proposed covering resulted in less solar heat absorption while the larger thermal emissivity led to more heat dissipation, making the proposed covering achieve the lowest stabilized temperature. The conventional heating material achieved the highest stabilized temperature mainly due to its much higher solar absorptance.

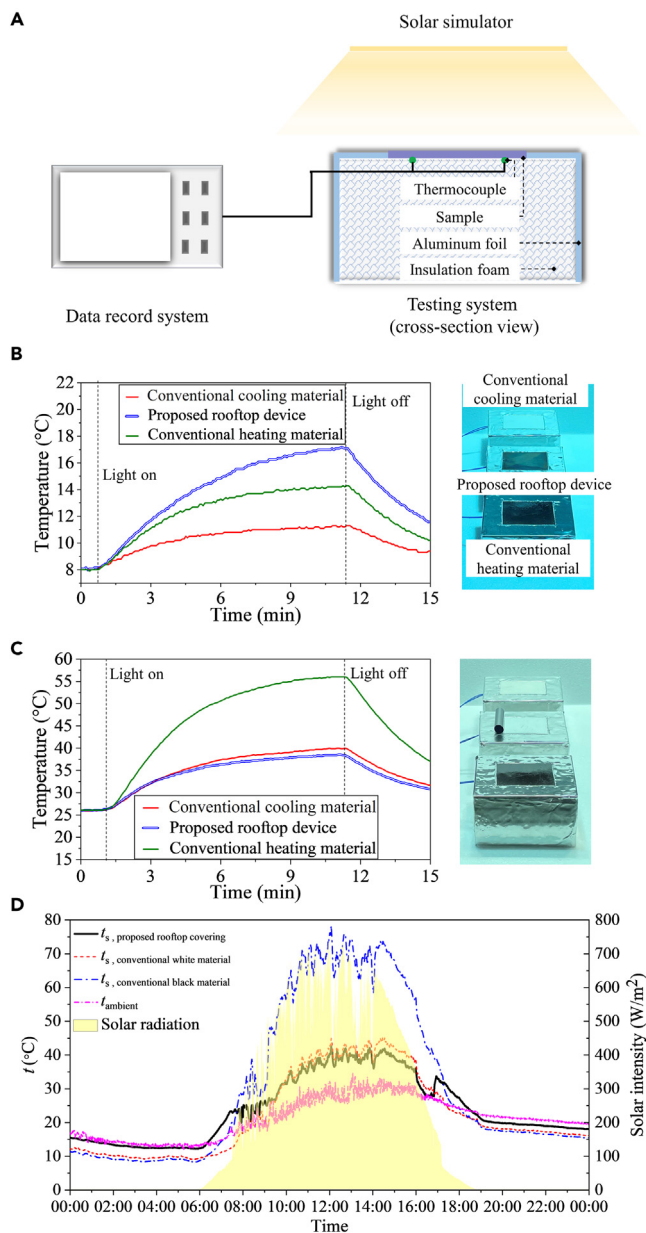


**Figure 3. Experimental tests of the proposed rooftop covering in regulating the roof surface temperature**

(A) Schematic of the experimental setup in simulated weather condition.

(B) (Left) roof surface temperature profiles of the three samples in simulated cold weather condition, and (right) the associated optical images at the stabilized state.

(C) (Left) roof surface temperature profiles of the three samples in simulated hot weather condition, and (right) the associated optical images at the stabilized state.

(D) Surface temperature ( $t_s$ ) of the proposed rooftop covering, conventional cooling and heating materials in outdoor environment recorded over a day-night cycle (the measurement was taken on Apr 05 2023 in Zhengzhou city (34.76°N 113.67°E)).

The outdoor experiments were also conducted to demonstrate the actual performance of the proposed device in real weather conditions. The experimental setup was shown in Figure S11. With reference to the existing studies,<sup>7,24,40,41</sup> a thin PE film with high hydrophobicity and solar and infrared transparency was covered above the proposed device to prevent it from wind disturbance and water/moisture environment. The results showed that the proposed device achieved higher and lower surface temperature than

both conventional heating and cooling materials in cold (e.g., 00:00 to 07:00) and hot (e.g., 10:00 to 16:00) time, respectively (Figure 3D), indicating excellent building energy-saving potentials. Furthermore, we tested the mechanical and optical properties of the proposed device before and after a longtime outdoor application (60 days, from Apr 06 2023 to Jun 05 2023 in Zhengzhou city). The results showed that the bending curvature, solar absorptance, and thermal emissivity of the device changed little after longtime outdoor application (Figure S12), indicating high stability and durability.

Overall, owing to the temperature-adaptive solar absorptance and thermal emissivity, the proposed rooftop covering achieved higher roof surface temperature than the conventional heating and cooling materials in cold seasons, while it achieved lower roof surface temperature than the two in hot seasons. Such excellent temperature-regulation capabilities would help reduce both building heating and cooling needs in practice.

### Building energy simulation

Building energy simulations were performed to quantify the energy-saving potentials of the proposed rooftop covering in different climate regions of China. Five cities were selected to represent these climate regions (Figure 4A), i.e., Harbin (severe cold), Beijing (cold), Wuhan (hot summer and cold winter), Kunming (warm/mild), and Hong Kong (hot summer and warm winter). In each city, an office building was built on the EnergyPlus platform and its configurations were set according to the design standard.<sup>60</sup> Based on the local weather file derived from the weather database of EnergyPlus, we firstly calculated the temperature of the heating material of the rooftop covering. Correspondingly, the solar absorptance and thermal emissivity of the rooftop covering were identified. The roof surface temperature of building can be further estimated, and it was adopted to calculate the heating/cooling degrees that quantified the difference between roof surface temperature and indoor temperature heating/cooling setpoints. Lastly, the building energy-saving potentials can be estimated using the regression relationship between the annual accumulated heating/cooling degrees and the annual heating/cooling energy savings.<sup>24,61</sup>

Here, we chose Wuhan as an example to analyze the identified optical properties, roof surface temperature, and building energy savings. As expected, large solar absorptance but small thermal emissivity was mainly identified in cold time including cold seasons and nighttime of transition seasons (Figures 4B and 4C) according to the quantified temperature of the heating material (Figure S13). By contrast, small solar absorptance but large thermal emissivity was identified in hot time (e.g., from June to August). Correspondingly, the proposed covering showed higher roof surface temperature  $t_{\text{proposed}}$  than both conventional heating ( $t_{\text{conventional heating}}$ ) and cooling ( $t_{\text{conventional cooling}}$ ) roof materials mainly in cold time, while lower surface temperature than the two in hot time (Figures 4D and 4E). Particularly, as the solar absorptance of the proposed covering was much smaller than that of the conventional heating material in hot time, it resulted in significant surface temperature decrease (up to 25.6°C decrease), indicating huge cooling energy-saving potentials. Taking the conventional heating and cooling roof materials as baselines, respectively, the monthly energy savings of the proposed rooftop covering were estimated, and they all showed positive values (Figure 4F). In cold season (e.g., January, February, and December), the proposed material achieved higher energy savings in comparison with the cooling material mainly because the former absorbed more solar heat and blocked infrared heat loss, resulting in less heating loads. In hot season (e.g., June, July, and August), the proposed covering achieved much higher cooling energy savings in comparison with the heating material mainly because the former largely reflected the solar heat and led to less building cooling loads. In total, the proposed covering achieved annual energy savings of 128 and 72 MJ/m<sup>2</sup> in comparison with the conventional heating and cooling materials, respectively.

Lastly, the annual energy savings of the five selected cities were quantified (Figure 4G), and three features can be drawn. First, the proposed rooftop covering achieved positive energy savings in comparison with both conventional heating and cooling roof materials in all the five selected cities. Second, Kunming and Harbin achieved the largest and smallest energy savings among the five cities, respectively, when taking the conventional heating material as baseline. Kunming experienced warm climate all year round and more critically, it was located on Yunnan-Guizhou Plateau which showed much richer solar resources than other regions. As the proposed covering presented much lower solar absorptance than the heating material especially in hot seasons, it significantly reduced the cooling loads derived from the solar heating and achieved the largest energy savings. Harbin was in severe cold region, and it experienced longer cold time and lower ambient temperature than other cities. In very cold time, the upper heating material of the

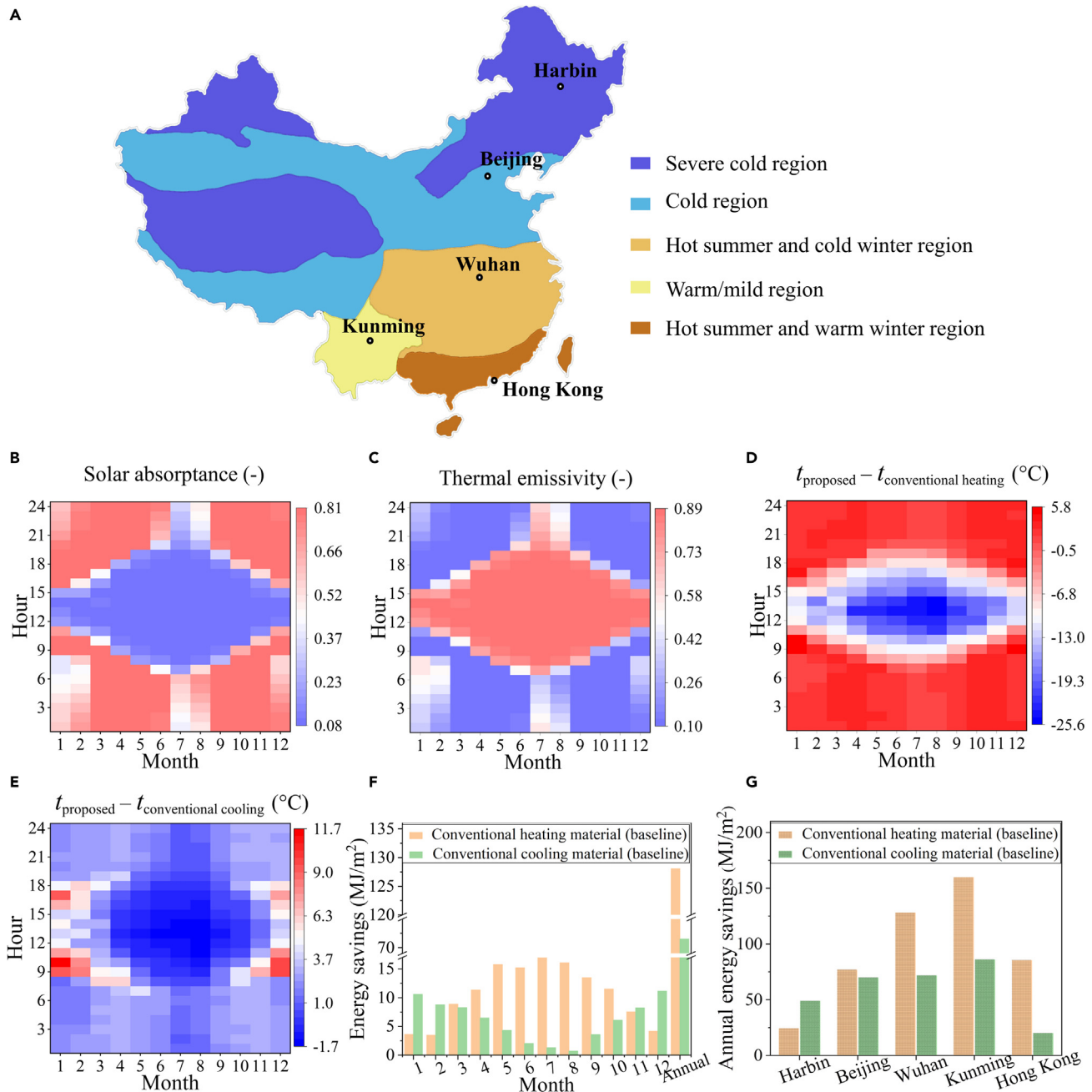


**Figure 4. Building energy savings of the proposed rooftop covering in different climate regions**

(A) Classification of Chinese climate regions and the five selected cities.

(B) Identified solar absorptance and (C) thermal emissivity of the proposed rooftop covering of Wuhan. Roof surface temperature differences between the proposed rooftop covering and the conventional.

(D) heating roof material, and (E) cooling roof material of Wuhan.

(F) Monthly and annual energy savings of the proposed rooftop covering of Wuhan.

(G) Annual energy savings of the five cities.

covering would bend toward the lower cooling material rather than the ambient at lower temperature (e.g., 5°C shown in Figure S14), which led to decreased solar absorptance and increased thermal emissivity, resulting in limited energy savings. This was mainly because the supporting force from the ground cannot offset the bending force of the heating material toward the ground so that the film cannot keep flat. Third,

Kunming and Hong Kong achieved the largest and smallest energy savings among the five cities, respectively, when taking the conventional cooling material as baseline. As discussed earlier, Kunming achieved the largest energy savings mainly due to its richer solar resources than other regions. Hong Kong was in hot summer and warm winter region, and heating energy use accounted for a very small proportion of annual energy use. Thus, the proposed covering achieved very limited heating energy savings. In addition, Hong Kong was humid especially in hot seasons, which would reduce the sky radiative cooling effects,<sup>62</sup> and lead to limited cooling energy savings.

## DISCUSSION

In this work, we developed surface temperature-adaptive rooftop covering with synergetic modulation of solar and thermal radiation for maximum energy savings, which achieved excellent solar absorptance modulation of 72.5% and thermal emissivity modulation of 79%. Such synergetic modulation was mainly enabled via thermal-induced bending actuation of a metalized PE film. Owing to the synergetic modulation, the proposed rooftop covering can induce solar heating and suppress infrared heat loss to reduce building heating loads in cold seasons, while it can reflect unwanted solar heat and enhance heat dissipation to reduce building cooling loads in hot seasons. Building simulation illustrated that the proposed covering achieved year-round energy savings in all climate regions. The covering was also scalable as it was fabricated using commonly used materials (e.g., PE film, zinc) via easy-to-be-implemented processes (electroplating, dipping). In all, this work opens pathway to achieve surface temperature-adaptive synergetic modulation of solar and thermal radiation for building applications. We foresee that this concept can be applied to other fields where radiation modulation is required under different temperatures, such as outdoor personal thermal management,<sup>42,43</sup> solar heat storage system.<sup>44</sup> Mentioned that when temperature is lower than 10°C, the upper heating material of the covering would bend toward the lower cooling material rather than the ambient, resulting in limited heating performance. To prevent this phenomenon, we propose to replace the PE film using the temperature-responsive liquid crystal,<sup>63</sup> which changes its length at high temperature but keeps fixed length at low temperature. Consequently, the rooftop covering will keep flat and will not bend toward the cooling material in cold environment. As the initial cost of the liquid crystal is much higher than that of the PE film and the liquid crystal cannot be recycled, it should be well considered when replacing the PE film using the liquid crystal in practice.

## Limitations of the study

There are two main limitations of this work. First, it requires high initial cost and manufacturing time. It takes 30 min to reach the required vacuum level for the magnetron sputtering, while it takes 8 min to deposit a very thin copper layer (~5 nm) onto the PE film. Then, 5 min are taken to electrodeposit a thick layer of zinc (~1000 nm) onto the electroconductive PE film. The metalized film is further dipped into a CuSO<sub>4</sub> solution for 40 s. It takes another 38 min to coat copper layer (~5 nm thickness) onto another side of the PE film. The whole process takes about 82 min. The sputtering is charged 100 HKD (~25 USD), while the other cost is only 10 HKD (~1.25 USD). Future work should explore fabrication methods to avoid the vacuum tools for reducing the manufacturing time and costs. Second, at low temperature, although the metalized PE film (upper layer) can cover the whole BaSO<sub>4</sub> paint (bottom layer) for heating, the thermal contact between the upper and bottom layers may not be good enough due to the existence of air gap, thereby hampering the heating performance of the proposed device. It is an inherent issue of this work and needs further investigation.

## STAR★METHODS

Detailed methods are provided in the online version of this paper and include the following:

- [KEY RESOURCES TABLE](#)
- [RESOURCE AVAILABILITY](#)
  - Lead contact
  - Materials availability
  - Data and code availability
- [EXPERIMENTAL MODEL AND SUBJECT DETAILS](#)
- [METHOD DETAILS](#)
  - Preparation of the temperature-responsive heating material
  - Bending property measurement
  - Finite-element modeling of the temperature-responsive material

- Preparation of roof surface temperature measurements
- Building simulation using EnergyPlus
- Measurements of linear thermal expansion ratio
- **QUANTIFICATION AND STATISTICAL ANALYSIS**
  - Identification of the optimal optical properties
  - Bending curvature calculation of the temperature-responsive heating material
  - Quantification of temperature-adaptive optical properties of the proposed rooftop covering
  - Estimations of building energy savings
  - Quantification of solar and thermal optical properties
- **ADDITIONAL RESOURCES**

## SUPPLEMENTAL INFORMATION

Supplemental information can be found online at <https://doi.org/10.1016/j.isci.2023.107388>.

## ACKNOWLEDGMENTS

The authors would like to acknowledge the funding support of The Hong Kong Polytechnic University through a Project of Strategic Importance (Project No: ZE1H). Special thanks go to the Surface engineering unit of the Additive manufacturing stream, Industrial Center (IC) of The Hong Kong Polytechnic University (HKPU) for helping the material preparation.

## AUTHOR CONTRIBUTIONS

J.-L.C. and J.-T.F. conceived the idea and planned the work. J.-L.C. conducted the experiments and theoretical calculation/numerical simulation. J.-H.C. and L.L. assisted the roof surface temperature tests, optical property measurements and provided advice on building simulation. Z.-X.K. conducted the finite-element modeling. C.-H.T. assisted the heating material fabrication. All the authors contributed the writing of the paper.

## DECLARATION OF INTERESTS

The authors declare no competing financial interests.

## INCLUSION AND DIVERSITY

We support inclusive, diverse, and equitable conduct of research.

Received: January 30, 2023

Revised: June 21, 2023

Accepted: July 11, 2023

Published: July 13, 2023

## REFERENCES

1. Zhao, H.-x., and Magoulès, F. (2012). A review on the prediction of building energy consumption. *Renew. Sustain. Energy Rev.* 16, 3586–3592. <https://doi.org/10.1016/j.rser.2012.02.049>.
2. Pérez-Lombard, L., Ortiz, J., and Pout, C. (2008). A review on buildings energy consumption information. *Energy Build.* 40, 394–398. <https://doi.org/10.1016/j.enbuild.2007.03.007>.
3. Sadineni, S.B., Madala, S., and Boehm, R.F. (2011). Passive building energy savings: a review of building envelope components. *Renew. Sustain. Energy Rev.* 15, 3617–3631. <https://doi.org/10.1016/j.rser.2011.07.014>.
4. Zeyghami, M., Goswami, D.Y., and Stefanakos, E. (2018). A review of clear sky radiative cooling developments and applications in renewable power systems and passive building cooling. *Sol. Energy Mater. Sol. Cell.* 178, 115–128. <https://doi.org/10.1016/j.solmat.2018.01.015>.
5. Chai, J., and Fan, J. (2022). Solar and thermal radiation-modulation materials for building applications. *Adv. Energy Mater.* 2202932. <https://doi.org/10.1002/aenm.202202932>.
6. Mandal, J., Fu, Y., Overvig, A.C., Jia, M., Sun, K., Shi, N.N., Zhou, H., Xiao, X., Yu, N., and Yang, Y. (2018). Hierarchically porous polymer coatings for highly efficient passive daytime radiative cooling. *Science* 362, 315–319. <https://doi.org/10.1126/science.aat9513>.
7. Zhai, Y., Ma, Y., David, S.N., Zhao, D., Lou, R., Tan, G., Yang, R., and Yin, X. (2017). Scalable-manufactured randomized glass-polymer hybrid metamaterial for daytime radiative cooling. *Science* 355, 1062–1066. <https://doi.org/10.1126/science.aai7899>.
8. Li, T., Zhai, Y., He, S., Gan, W., Wei, Z., Heidarinejad, M., Dalgo, D., Mi, R., Zhao, X., Song, J., et al. (2019). A radiative cooling structural material. *Science* 364, 760–763. <https://doi.org/10.1126/science.aau9101>.
9. Bijarniya, J.P., Sarkar, J., and Maiti, P. (2020). Review on passive daytime radiative cooling: fundamentals, recent researches, challenges and opportunities. *Renew. Sustain. Energy Rev.* 133, 110263. <https://doi.org/10.1016/j.rser.2020.110263>.
10. Mandal, J., Du, S., Dontigny, M., Zaghbi, K., Yu, N., and Yang, Y. (2018). Li4Ti5O12: a visible-to-infrared broadband electrochromic material for optical and thermal

- management. *Adv. Funct. Mater.* 28, 1802180. <https://doi.org/10.1002/adfm.201802180>.
11. Ke, Y., Li, Y., Wu, L., Wang, S., Yang, R., Yin, J., Tan, G., and Long, Y. (2022). On-demand solar and thermal radiation management based on switchable interwoven surfaces. *ACS Energy Lett.* 7, 1758–1763. <https://doi.org/10.1021/acsenenergylett.2c00419>.
  12. Rao, Y., Dai, J., Sui, C., Lai, Y.-T., Li, Z., Fang, H., Li, X., Li, W., and Hsu, P.-C. (2021). Ultra-wideband transparent conducting electrode for electrochromic synergistic solar and radiative heat management. *ACS Energy Lett.* 6, 3906–3915. <https://doi.org/10.1021/acsenenergylett.1c01486>.
  13. Li, X., Sun, B., Sui, C., Nandi, A., Fang, H., Peng, Y., Tan, G., and Hsu, P.-C. (2020). Integration of daytime radiative cooling and solar heating for year-round energy saving in buildings. *Nat. Commun.* 11, 6101. <https://doi.org/10.1038/s41467-020-19790-x>.
  14. Wang, W., Zou, Q., Wang, N., Hong, B., Zhang, W., and Wang, G.P. (2021). Janus multilayer for radiative cooling and heating in double-side photonic thermal system. *ACS Appl. Mater. Interfaces* 13, 42813–42821. <https://doi.org/10.1021/acsaami.1c11552>.
  15. Song, Y.-N., Lei, M.-Q., Han, D.-L., Huang, Y.-C., Wang, S.-P., Shi, J.-Y., Li, Y., Xu, L., Lei, J., and Li, Z.-M. (2021). Multifunctional membrane for thermal management applications. *ACS Appl. Mater. Interfaces* 13, 19301–19311. <https://doi.org/10.1021/acsaami.1c02667>.
  16. Wang, T., Zhang, Y., Chen, M., Gu, M., and Wu, L. (2022). Scalable and waterborne titanium-dioxide-free thermochromic coatings for self-adaptive passive radiative cooling and heating. *Cell Rep. Phys. Sci.* 3, 100782. <https://doi.org/10.1016/j.xcrp.2022.100782>.
  17. Zhu, Y., Wang, C., and Guo, X. (2019). Smart utilization of solar energy with Optic-Variable Wall (OVW) for thermal comfort. *Energy Build.* 202, 109376. <https://doi.org/10.1016/j.enbuild.2019.109376>.
  18. Karlessi, T., Santamouris, M., Apostolakis, K., Synnefa, A., and Livada, I. (2009). Development and testing of thermochromic coatings for buildings and urban structures. *Sol. Energy* 83, 538–551. <https://doi.org/10.1016/j.solener.2008.10.005>.
  19. Yuxuan, Z., Yunyun, Z., Jianrong, Y., and Xiaoqiang, Z. (2020). Energy saving performance of thermochromic coatings with different colors for buildings. *Energy Build.* 215, 109920. <https://doi.org/10.1016/j.enbuild.2020.109920>.
  20. Perez, G., Allegro, V.R., Corroto, M., Pons, A., and Guerrero, A. (2018). Smart reversible thermochromic mortar for improvement of energy efficiency in buildings. *Construct. Build. Mater.* 186, 884–891. <https://doi.org/10.1016/j.conbuildmat.2018.07.246>.
  21. Zheng, S., Xu, Y., Shen, Q., and Yang, H. (2015). Preparation of thermochromic coatings and their energy saving analysis. *Sol. Energy* 112, 263–271. <https://doi.org/10.1016/j.solener.2014.09.049>.
  22. Berardi, U., Garai, M., and Morselli, T. (2020). Preparation and assessment of the potential energy savings of thermochromic and cool coatings considering inter-building effects. *Sol. Energy* 209, 493–504. <https://doi.org/10.1016/j.solener.2020.09.015>.
  23. Zhang, W.-W., Qi, H., Sun, A.-T., Ren, Y.-T., and Shi, J.-W. (2020). Periodic trapezoidal VO<sub>2</sub>-Ge multilayer absorber for dynamic radiative cooling. *Opt. Express* 28, 20609–20623. <https://doi.org/10.1364/oe.396171>.
  24. Tang, K., Dong, K., Li, J., Gordon, M.P., Reichertz, F.G., Kim, H., Rho, Y., Wang, Q., Lin, C.-Y., Grigoropoulos, C.P., et al. (2021). Temperature-adaptive radiative coating for all-season household thermal regulation. *Science* 374, 1504–1509. <https://doi.org/10.1126/science.abf7136>.
  25. Araki, K., and Zhang, R.Z. (2022). An optimized self-adaptive thermal radiation turn-down coating with vanadium dioxide nanowire array. *Int. J. Heat Mass Tran.* 191, 122835. <https://doi.org/10.1016/j.ijheatmasstransfer.2022.122835>.
  26. Taylor, S., Yang, Y., and Wang, L. (2017). Vanadium dioxide based Fabry-Perot emitter for dynamic radiative cooling applications. *J. Quant. Spectrosc. Radiat. Transf.* 197, 76–83. <https://doi.org/10.1016/j.jqsrt.2017.01.014>.
  27. Taylor, S., Long, L., McBurney, R., Sabbaghi, P., Chao, J., and Wang, L. (2020). Spectrally-selective vanadium dioxide based tunable metafilm emitter for dynamic radiative cooling. *Sol. Energy Mater. Sol. Cell.* 217, 110739. <https://doi.org/10.1016/j.solmat.2020.110739>.
  28. Ito, K., Watari, T., Nishikawa, K., Yoshimoto, H., and Iizuka, H. (2018). Inverting the thermal radiative contrast of vanadium dioxide by metasurfaces based on localized gap-plasmons. *APL Photonics* 3, 086101. <https://doi.org/10.1063/1.5025947>.
  29. Ono, M., Chen, K., Li, W., and Fan, S. (2018). Self-adaptive radiative cooling based on phase change materials. *Opt. Express* 26, A777–A787. <https://doi.org/10.1364/OE.26.00A777>.
  30. Qu, Y., Li, Q., Cai, L., Pan, M., Ghosh, P., Du, K., and Qiu, M. (2018). Thermal camouflage based on the phase-changing material GST. *Light Sci. Appl.* 7, 26. <https://doi.org/10.1038/s41377-018-0038-5>.
  31. Cai, L., Du, K., Qu, Y., Luo, H., Pan, M., Qiu, M., and Li, Q. (2018). Nonvolatile tunable silicon-carbide-based midinfrared thermal emitter enabled by phase-changing materials. *Opt. Lett.* 43, 1295–1298. <https://doi.org/10.1364/OL.43.001295>.
  32. Hua, X., and Zheng, G. (2019). Intensity switchable and wide-angle mid-infrared perfect absorber with lithography-free phase-change film of Ge<sub>2</sub>Sb<sub>2</sub>Te<sub>5</sub>. *Micromachines* 10, 374. <https://doi.org/10.3390/mi10060374>.
  33. Douglas, H.W., Theresa, S.M., Clara, R.-B., Nikolas, P., Kathleen, R., Jeremy, T., Alexej, P., Musgraves, J.D., Jeremy, A.B., Hee Jung, S., et al. (2011). Adaptive Phase Change Metamaterials for Infrared Aperture Control. <https://doi.org/10.1117/12.894892>.
  34. Huang, J., Xuan, Y., and Li, Q. (2011). Perovskite-type oxide films combined with gratings for reduction of material consumption and improvement of thermochromism property. *J. Quant. Spectrosc. Radiat. Transf.* 112, 2592–2599. <https://doi.org/10.1016/j.jqsrt.2011.07.012>.
  35. Tachikawa, S., Ohnishi, A., Shimakawa, Y., Ochi, A., Okamoto, A., and Nakamura, Y. (2003). Development of a variable emittance radiator based on a perovskite manganese oxide. *J. Thermophys. Heat Tran.* 17, 264–268. <https://doi.org/10.2514/2.6760>.
  36. Fan, D., Li, Q., Xuan, Y., Tan, H., and Fang, J. (2013). Temperature-dependent infrared properties of Ca doped (La,Sr)MnO<sub>3</sub> compositions with potential thermal control application. *Appl. Therm. Eng.* 51, 255–261. <https://doi.org/10.1016/j.applthermaleng.2012.07.046>.
  37. Fan, D., Li, Q., and Dai, P. (2016). Temperature-dependent emissivity property in La<sub>0.7</sub>Sr<sub>0.3</sub>MnO<sub>3</sub> films. *Acta Astronaut.* 121, 144–152. <https://doi.org/10.1016/j.actaastro.2016.01.001>.
  38. Shen, X., Li, L., Wu, X., Gao, Z., and Xu, G. (2011). Infrared emissivity of Sr doped lanthanum manganites in coating form. *J. Alloys Compd.* 509, 8116–8119. <https://doi.org/10.1016/j.jallcom.2011.05.072>.
  39. Wang, W., Zhao, Z., Zou, Q., Hong, B., Zhang, W., and Wang, G.P. (2020). Self-adaptive radiative cooling and solar heating based on a compound metasurface. *J. Mater. Chem. C Mater.* 8, 3192–3199. <https://doi.org/10.1039/C9TC05634C>.
  40. Zhang, Q., Wang, Y., Lv, Y., Yu, S., and Ma, R. (2022). Bioinspired zero-energy thermal-management device based on visible and infrared thermochromism for all-season energy saving. *Proc. Natl. Acad. Sci. USA* 119, e2207353119. <https://doi.org/10.1073/pnas.2207353119>.
  41. Zhang, Q., Lv, Y., Wang, Y., Yu, S., Li, C., Ma, R., and Chen, Y. (2022). Temperature-dependent dual-mode thermal management device with net-zero energy for year-round energy saving. *Nat. Commun.* 13, 4874. <https://doi.org/10.1038/s41467-022-32528-1>.
  42. Luo, H., Zhu, Y., Xu, Z., Hong, Y., Ghosh, P., Kaur, S., Wu, M., Yang, C., Qiu, M., and Li, Q. (2021). Outdoor personal thermal management with simultaneous electricity generation. *Nano Lett.* 21, 3879–3886. <https://doi.org/10.1021/acs.nanolett.1c00400>.
  43. Hsu, P.-C., Liu, C., Song, A.Y., Zhang, Z., Peng, Y., Xie, J., Liu, K., Wu, C.-L., Cattrysse, P.B., Cai, L., et al. (2017). A dual-mode textile for human body radiative heating and cooling. *Sci. Adv.* 3, e1700895. <https://doi.org/10.1126/sciadv.1700895>.

44. Liu, R., Li, J., Duan, J., Yu, B., Xie, W., Qi, B., Wang, H., Zhuang, X., Liu, S., Liu, P., et al. (2021). High-efficiency solar heat storage enabled by adaptive radiation management. *Cell Rep. Phys. Sci.* 2, 100533. <https://doi.org/10.1016/j.xcrp.2021.100533>.
45. Kant, K., and Pitchumani, R. (2022). Advances and opportunities in thermochemical heat storage systems for buildings applications. *Appl. Energy* 321, 119299. <https://doi.org/10.1016/j.apenergy.2022.119299>.
46. Orchard, G.A.J., Davies, G.R., and Ward, I.M. (1984). The thermal expansion behaviour of highly oriented polyethylene. *Polymer* 25, 1203–1210. [https://doi.org/10.1016/0032-3861\(84\)90364-1](https://doi.org/10.1016/0032-3861(84)90364-1).
47. Ladizesky, N.H., and Ward, I.M. (1971). Determination of Poisson's ratio and Young's modulus of low-density polyethylene. *J. Macromol. Sci., Part B* 5, 661–692. <https://doi.org/10.1080/00222347108224781>.
48. Ledbetter, H.M. (1977). Elastic properties of zinc: a compilation and a review. *J. Phys. Chem. Ref. Data* 6, 1181–1203. <https://doi.org/10.1063/1.555564>.
49. Ledbetter, H.M., and Naimon, E.R. (2009). Elastic properties of metals and alloys. II. copper. *J. Phys. Chem. Ref. Data* 3, 897–935. <https://doi.org/10.1063/1.3253150>.
50. Mallory, G.O., and Hajdu, J.B. (1990). *Electroless Plating: Fundamentals and Applications (William Andrew)*.
51. Kanani, N. (2004). *Electroplating: Basic Principles, Processes and Practice (Elsevier)*.
52. Mandal, J., Wang, D., Overvig, A.C., Shi, N.N., Paley, D., Zangiabadi, A., Cheng, Q., Barmak, K., Yu, N., and Yang, Y. (2017). Scalable, "Dip-and-Dry" fabrication of a wide-angle plasmonic selective absorber for high-efficiency solar-thermal energy conversion. *Adv. Mater.* 29, 1702156. <https://doi.org/10.1002/adma.201702156>.
53. Thermostats. U.S. Department of Energy. [www.energy.gov/energysaver/thermostats](http://www.energy.gov/energysaver/thermostats).
54. Li, X., Peoples, J., Yao, P., and Ruan, X. (2021). Ultrawhite BaSO<sub>4</sub> paints and films for remarkable daytime subambient radiative cooling. *ACS Appl. Mater. Interfaces* 13, 21733–21739. <https://doi.org/10.1021/acscami.1c02368>.
55. Li, X., Ma, B., Dai, J., Sui, C., Pande, D., Smith, D.R., Brinson, L.C., and Hsu, P.-C. (2021). Metalized polyamide heterostructure as a moisture-responsive actuator for multimodal adaptive personal heat management. *Sci. Adv.* 7, eabj7906. <https://doi.org/10.1126/sciadv.abj7906>.
56. Wang, W., Yao, L., Cheng, C.-Y., Zhang, T., Atsumi, H., Wang, L., Wang, G., Anilonyte, O., Steiner, H., Ou, J., et al. (2017). Harnessing the hygroscopic and biofluorescent behaviors of genetically tractable microbial cells to design biohybrid wearables. *Sci. Adv.* 3, e1601984. <https://doi.org/10.1126/sciadv.1601984>.
57. Baneshi, M., Maruyama, S., and Komiya, A. (2011). Comparison between aesthetic and thermal performances of copper oxide and titanium dioxide nano-particulate coatings. *J. Quant. Spectrosc. Radiat. Transf.* 112, 1197–1204. <https://doi.org/10.1016/j.jqsrt.2010.08.032>.
58. Qi, Y., Xiang, B., and Zhang, J. (2017). Effect of titanium dioxide (TiO<sub>2</sub>) with different crystal forms and surface modifications on cooling property and surface wettability of cool roofing materials. *Sol. Energy Mater. Sol. Cell.* 172, 34–43. <https://doi.org/10.1016/j.solmat.2017.07.017>.
59. Abdelkader, T.K., Zhang, Y., Gaballah, E.S., Wang, S., Wan, Q., and Fan, Q. (2020). Energy and exergy analysis of a flat-plate solar air heater coated with carbon nanotubes and cupric oxide nanoparticles embedded in black paint. *J. Clean. Prod.* 250, 119501. <https://doi.org/10.1016/j.jclepro.2019.119501>.
60. Hong, T., Li, C., and Yan, D. (2015). Updates to the China design standard for energy efficiency in public buildings. *Energy Pol.* 87, 187–198. <https://doi.org/10.1016/j.enpol.2015.09.013>.
61. Rosado, P.J., and Levinson, R. (2019). Potential benefits of cool walls on residential and commercial buildings across California and the United States: conserving energy, saving money, and reducing emission of greenhouse gases and air pollutants. *Energy Build.* 199, 588–607. <https://doi.org/10.1016/j.enbuild.2019.02.028>.
62. Yin, X., Yang, R., Tan, G., and Fan, S. (2020). Terrestrial radiative cooling: using the cold universe as a renewable and sustainable energy source. *Science* 370, 786–791. <https://doi.org/10.1126/science.abb0971>.
63. Saha, R.K., Torbati, A.H., and Frick, C.P. (2021). Body-temperature shape-shifting liquid crystal elastomers. *J. Appl. Polym. Sci.* 138, 50136. <https://doi.org/10.1002/app.50136>.
64. Nix, F.C., and MacNair, D. (1941). The thermal expansion of pure metals: copper, gold, aluminum, nickel, and iron. *Phys. Rev.* 60, 597–605. <https://doi.org/10.1103/PhysRev.60.597>.
65. Rychlewski, J. (1984). On Hooke's law. *J. Appl. Math. Mech.* 48, 303–314. [https://doi.org/10.1016/0021-8928\(84\)90137-0](https://doi.org/10.1016/0021-8928(84)90137-0).
66. Hsueh, C.H., and Evans, A.G. (1985). Residual stresses in meta/ceramic bonded strips. *J. Am. Ceram. Soc.* 68, 241–248. <https://doi.org/10.1111/j.1151-2916.1985.tb15316.x>.
67. Hsueh, C.-H. (2002). Modeling of elastic deformation of multilayers due to residual stresses and external bending. *J. Appl. Phys.* 91, 9652–9656. <https://doi.org/10.1063/1.1478137>.
68. Nikishkov, G.P. (2003). Curvature estimation for multilayer hinged structures with initial strains. *J. Appl. Phys.* 94, 5333–5336. <https://doi.org/10.1063/1.1610777>.
69. Qin, Y., and Hiller, J.E. (2013). Ways of formulating wind speed in heat convection significantly influencing pavement temperature prediction. *Heat Mass Tran.* 49, 745–752. <https://doi.org/10.1007/s00231-013-1116-0>.
70. Evangelisti, L., Guattari, C., and Asdrubali, F. (2019). On the sky temperature models and their influence on buildings energy performance: A critical review. *Energy Build.* 183, 607–625. <https://doi.org/10.1016/j.enbuild.2018.11.037>.
71. Modest, M.F., and Mazumder, S. (2021). *Radiative Heat Transfer (Academic press)*.

## STAR★METHODS

### KEY RESOURCES TABLE

REAGENT or RESOURCE	SOURCE	IDENTIFIER
Chemicals, peptides, and recombinant proteins		
Low-density polyethylene film	Wangshi packaging Co. Ltd.	NA
Copper target	SANTE metal	NA
Barium sulfate	Macklin	CAS#7727-43-7
Zinc sulfate	Dieckmann	CAS#7446-20-0
Sulfuric acid	Sigma Aldrich	CAS#7664-93-9
Copper sulfate	Sigma Aldrich	CAS#7758-98-7
Software and algorithms		
ABAQUS	3DEXPERIENCE Company	<a href="https://www.3ds.com/products-services/simulia/products/abaqus/">https://www.3ds.com/products-services/simulia/products/abaqus/</a>
EnergyPlus	Department of Energy of US	<a href="https://energyplus.net/">https://energyplus.net/</a>

### RESOURCE AVAILABILITY

#### Lead contact

Further information and any related requests should be directed to and will be fulfilled by the lead contact, Prof. Fan Jintu ([jin-tu.fan@polyu.edu.hk](mailto:jin-tu.fan@polyu.edu.hk)).

#### Materials availability

This study did not generate new materials.

#### Data and code availability

- All data reported in this paper will be shared by the [lead contact](#) upon reasonable request.
- This paper does not report original code.
- Any additional information required to reanalyze the data reported in this paper is available from the [lead contact](#) upon reasonable request.

### EXPERIMENTAL MODEL AND SUBJECT DETAILS

There are no experimental model and subject details to be reported.

### METHOD DETAILS

#### Preparation of the temperature-responsive heating material

A very thin copper layer (~5 nm) was firstly deposited onto the polyethylene (PE) film using magnetron sputtering (MAT 400). The coating thickness was controlled by tuning the sputtering power and time. Then, a thick layer of zinc (~1000 nm) was electrodeposited onto the electroconductive film. The plating bath contained 350 g/L zinc sulfate (99%, Dieckmann), 25 g/L sulfuric acid (99.5%, Sigma Aldrich), and 20 mL/L additive (Bigely, 99%). The layer thickness was controlled by tuning the input current and plating time. The metalized film was further dipped into a copper sulfate (CuSO<sub>4</sub>) solution, washed using deionized (DI) water and dried. At last, a very thin layer (~5 nm) of copper was deposited onto another side of the PE film using magnetron sputtering.

#### Bending property measurement

The bending property of the temperature-responsive heating material was quantified within a small environmental chamber (YG(B)606G, Wenzhou Darong), which can maintain different cold and hot ambient temperatures. The sample was placed onto a white paper, and one end of the sample was fixed using glass

sheet. Optical images of the sample were taken at different temperatures of 10, 15, 20, 25, 30, 35, 40°C and 45°C respectively when the sample reached the thermal equilibrium state. We recorded the bending curvature and open-area ratio of the sample by analyzing the images using ImageJ software.

### Finite-element modeling of the temperature-responsive material

A three-dimensional finite-element model is constructed to demonstrate the bending actuation of the temperature-responsive material using the thermal module in the ABAQUS software. The material with simplified bilayer structure is rectangular, and one end of the material is fixed. The upper layer is the zinc metal with thickness of 1000 nm while the lower layer is the polyethylene (PE) film with thickness of 0.4 μm. The Young's modulus of the zinc layer and PE film are set as 105 Gpa, 0.2 Gpa respectively. The Poisson's ratio of the zinc layer and PE film are set as 0.38 and 0.4 respectively. The thermal expansion coefficients of the zinc layer and PE film are set according to the thermal expansion ratio and temperature difference.

### Preparation of roof surface temperature measurements

The test cell (13 cm × 10 cm × 8 cm) covered with aluminum foil was made using white extruded polystyrene (XPS) sheet. On the top surface of each test cell, a hole of 7.5 cm × 5.5 cm was cut from the foil and the sample was placed into the hole. Solar simulator (SOL 500/1200/2000) installed above the test cells were adopted to simulate the solar light. Two K-type thermocouples were installed onto the sample to measure the surface temperature, and the data were recorded using a data record system at a time interval of 5s.

### Building simulation using EnergyPlus

An office building (10 × 10 × 3 m) was built in EnergyPlus for each city. The indoor heating and cooling setpoints were set as 22°C and 25°C, respectively. The other configurations (e.g., U-value of envelope) of the building was set according to the design standard.<sup>60</sup> In each city, the typical meteorological year (TMY) weather data were derived from the weather database. The single-year building energy simulations were then conducted to obtain the roof surface temperature and building energy demands under different sets of roof optical properties. The results would be adopted to quantify the regression relationship between the accumulated heating/cooling degrees and the annual energy savings.

### Measurements of linear thermal expansion ratio

In this study, the thermal expansion ratio of the PE film (Figure S15) was measured using a thermal mechanical analyzer (Mettler Toledo TMA/SDTA1), while that of the metal layer was obtained from the ref. 48 and 64. The film was prepared in regular shape (20 mm × 4 mm) and attached onto two hooks along the length direction. During the test, a small tensile force of 0.05 N was applied on the film to ensure the film keep straight. The temperature scan was performed at 2°C/min. Taking the length at 20°C ( $l_{20}$ ) as a reference, the linear thermal expansion ratio at each temperature  $t$  was calculated as  $(l_t - l_{20})/l_{20}$ , where  $l_t$  is the length of film at temperature  $t$ . The thermal expansion coefficient used in the numerical simulation can be obtained according to the thermal expansion ratio and temperature difference.

## QUANTIFICATION AND STATISTICAL ANALYSIS

### Identification of the optimal optical properties

The solar absorptance affects the solar absorption of the material while the thermal emissivity affects the infrared heat loss of the material through sky radiative cooling. To identify the optimal solar absorptance and thermal emissivity, we assume the material to achieve thermal equilibrium under solar absorption and sky radiative cooling. The associated equations at the thermal equilibrium state are shown below.<sup>24</sup>

$$q_{\text{solar}} = q_{\text{thermal}} \quad (\text{Equation 1})$$

$$q_{\text{solar}} = A_{\text{ts}} \cdot I \quad (\text{Equation 2})$$

$$q_{\text{thermal}} = \epsilon_{\text{ts}} \cdot \sigma \left( (t_{\text{s}} + 273.15)^4 - (t_{\text{sky}} + 273.15)^4 \right) \quad (\text{Equation 3})$$

where,  $q_{\text{solar}}$  and  $q_{\text{thermal}}$  are the solar absorption and infrared heat loss through sky radiative cooling respectively.  $A_{\text{ts}}$  and  $I$  are the solar absorptance (unit: %) and the global solar radiation (unit: W/m<sup>2</sup>) respectively.

$\epsilon_{t_s}$  is the thermal emissivity (unit: %).  $\sigma$  is the Stefan-Boltzmann constant ( $5.670374419 \times 10^{-8} \text{ W/m}^2/\text{K}^4$ ).  $t_s$  and  $t_{sky}$  are the surface temperature (unit: °C) and sky temperature (unit: °C) respectively.

The global solar radiation and sky temperature of ( $200 \text{ W/m}^2, 0^\circ\text{C}$ ) and ( $800 \text{ W/m}^2, 25^\circ\text{C}$ ) are chosen as examples to identify the optimal optical properties of the heating material and cooling material, respectively. By substituting the known parameters into Equations 1, 2, and 3, the associated surface temperature can be obtained and the optimal optical properties will be identified accordingly.

### Bending curvature calculation of the temperature-responsive heating material

Figure S16 shows the schematic of the bended heating material at the equilibrium state. Note that as the Cu nanoclusters randomly disperse onto the Zn layer rather than forming dense metal layer,<sup>52</sup> they have little impacts on the bending properties of the heating material, and thus they are not considered in the theoretical analysis. The displacement constraint is set at one end of the structure (i.e., left end of the material in Figure S16). In each layer the relationship between normal stress  $\sigma$  and total strain  $\epsilon$  can be obtained using the Hooke's law.<sup>65</sup>

$$\sigma = E'(\epsilon - \nu'\epsilon^0) \quad (\text{Equation 4})$$

where,  $E'$  is equal to  $E/(1 - \nu^2)$ , in which  $E$  and  $\nu$  are the Young's modulus and Poisson's ratio respectively;  $\nu'$  is equal to  $1 + \nu$ ;  $\epsilon^0$  is the original strain before being restricted by the four-layer structure.

The total strain  $\epsilon$  in the four-layer structure is linearly proportional to the  $y$  coordinate as follows.<sup>66</sup>

$$\epsilon = \frac{y - y_a}{R} + b \quad (\text{Equation 5})$$

where,  $y_a$  is the  $y$  coordinate of the location where the bending strain component is zero;  $R$  is the bending radius of the four-layer structure;  $b$  is the uniform strain component.

The expression of the normal stress  $\sigma$  can be obtained by substituting Equation 5 into Equation 4.

$$\sigma = E' \left( \frac{y - y_a}{R} + b - \nu'\epsilon^0 \right) \quad (\text{Equation 6})$$

There are three unknown parameters including  $y_a$ ,  $b$  and  $R$ . As the structure is at equilibrium state, the force due to bending and uniform strains as well as the bending moment should be zero.<sup>67,68</sup> This leads to the three following equilibrium equations.

$$\sum_{i=1}^4 \int_{y_{i-1}}^{y_i} E_i \frac{(y - y_a)}{R} dy = 0 \quad (\text{Equation 7-1})$$

$$\sum_{i=1}^4 \int_{y_{i-1}}^{y_i} E_i (b - \nu'\epsilon_i^0) dy = 0 \quad (\text{Equation 7-2})$$

$$\sum_{i=1}^4 \int_{y_{i-1}}^{y_i} E_i \left( \frac{y - y_a}{R} + b - \nu'\epsilon_i^0 \right) (y - y_a) dy = 0 \quad (\text{Equation 7-3})$$

In the integration process,  $y_0, y_1, y_2, y_3$  and  $y_4$  are set as  $0, t_1, t_1+t_2, t_1+t_2+t_3$  and  $t_1+t_2+t_3+t_4$  respectively according to Figure S16. We obtain the solutions of parameters  $y_a, b$  and  $R$  by solving these equations.

$$y_a = \frac{\sum_{i=1}^4 E_i t_i (y_i + y_{i-1})}{2 \sum_{i=1}^4 E_i t_i} \quad (\text{Equation 8-1})$$

$$b = \frac{\sum_{i=1}^4 E_i t_i \nu' \epsilon_i^0}{\sum_{i=1}^4 E_i t_i} \quad (\text{Equation 8-2})$$

$$R = \frac{2\sum_{i=1}^4 E_i' t_i [y_i^2 + y_i y_{i-1} + y_{i-1}^2 - 3y_a(y_i + y_{i-1} - y_a)]}{3\sum_{i=1}^4 E_i' t_i (y_i + y_{i-1} - 2y_a)(b - \nu_i' \varepsilon_i^0)} \quad (\text{Equation 8-3})$$

After conducting complex algebraic transformations, we obtain the bending radius R of the four-layer structure as follows.

$$R = \frac{\left\{ E_1'^2 t_1^4 + E_2'^2 t_2^4 + E_3'^2 t_3^4 + E_4'^2 t_4^4 + 2E_1' E_2' t_1 t_2 \left[ 2(t_1 + t_2)^2 - t_1 t_2 \right] + 2E_1' E_3' t_1 t_3 \left[ 2(t_1 + t_3)^2 - t_1 t_3 6t_2(t_1 + t_2 + t_3) \right] \right. \\ \left. + 2E_1' E_4' t_1 t_4 \left[ 2(t_1 + t_4)^2 - t_1 t_4 + 6(t_2 + t_3)(t_1 + t_2 + t_3 + t_4) \right] + 2E_2' E_3' t_2 t_3 \left[ 2(t_2 + t_3)^2 - t_2 t_3 \right] \right. \\ \left. + 2E_2' E_4' t_2 t_4 \left[ 2(t_2 + t_4)^2 - t_2 t_4 + 6t_3(t_2 + t_3 + t_4) \right] + 2E_3' E_4' t_3 t_4 \left[ 2(t_3 + t_4)^2 - t_3 t_4 \right] \right\}}{6 \left[ E_1' E_2' t_1 t_2 (t_1 + t_2) (\nu_1' \varepsilon_1^0 - \nu_2' \varepsilon_2^0) + E_1' E_3' t_1 t_3 (t_1 + 2t_2 + t_3) (\nu_1' \varepsilon_1^0 - \nu_3' \varepsilon_3^0) + E_2' E_3' t_2 t_3 (t_2 + t_3) (\nu_2' \varepsilon_2^0 - \nu_3' \varepsilon_3^0) \right. \\ \left. + E_1' E_4' t_1 t_4 (t_1 + 2t_2 + 2t_3 + t_4) (\nu_1' \varepsilon_1^0 - \nu_4' \varepsilon_4^0) + E_2' E_4' t_2 t_4 (t_2 + 2t_3 + t_4) (\nu_2' \varepsilon_2^0 - \nu_4' \varepsilon_4^0) + E_3' E_4' t_3 t_4 (t_3 + t_4) (\nu_3' \varepsilon_3^0 - \nu_4' \varepsilon_4^0) \right]} \quad (\text{Equation 8-4})$$

where, the subscripts 1, 2, 3 and 4 represent the copper layer in the bottom, polyethylene film, copper layer above the polyethylene film, and zinc layer, respectively.

Last, the bending curvature K can be obtained using the following equation.

$$K = \frac{1}{R} \quad (\text{Equation 8-5})$$

### Quantification of temperature-adaptive optical properties of the proposed rooftop covering

The temperature-adaptive solar absorptance  $A_t$  and thermal emissivity  $\varepsilon_t$  of the proposed rooftop covering (Figure 1A) are jointly determined by the tailored optical properties of the heating and cooling materials (Figure 2B), and the temperature-dependent open-area ratio  $r_t$  (Figure 2F).  $A_t$  and  $\varepsilon_t$  are quantified using Equations 9 and 10. Particularly, when the temperature of the heating material is equal or higher than 30°C,  $A_t$  and  $\varepsilon_t$  will be quantified using the optical properties of the heating material of the back side (Figure S17) as the back faces the outside.

$$A_t = A_{\text{cooling}} \cdot r_t + A_{\text{heating}} \cdot (100\% - r_t) \quad (\text{Equation 9})$$

$$\varepsilon_t = \varepsilon_{\text{cooling}} \cdot r_t + \varepsilon_{\text{heating}} \cdot (100\% - r_t) \quad (\text{Equation 10})$$

where,  $A_{\text{cooling}}$  and  $A_{\text{heating}}$  are the solar absorptance of cooling and heating materials respectively, while  $\varepsilon_{\text{cooling}}$  and  $\varepsilon_{\text{heating}}$  are the thermal emissivity of cooling and heating materials respectively.

When temperature is lower than 10°C, the polyethylen (PE) film would largely contract and make the heating material bend toward the cooling material rather than the ambient (Figure S14). In this case, part of the cooling material would expose to the ambient, resulting in decreased solar absorptance and increased thermal emissivity for the proposed covering. With the further decrease of temperature, the PE film would further contract and the bending curvature (absolute value) of the heating material would again increase according the theoretical analysis. Here we assume the bending curvature of the heating material at temperature 5°C or lower value would reproduce the curvature at temperature 25°C or higher value, and the associated open-area ratio at the temperature of -15°C-5°C is symmetrical to that at the temperature of 25°C-45°C. We measured the open-area ratios of the covering at the temperature of 0°C (81%) and 5°C (5.5%), and found they agreed well with the assumed results at 0°C (76.7%) and 5°C (4.0%). Thus, we consider the assumption is reliable, and utilize such estimated open-area ratios (Figure S18A) to quantify the optical properties of the rooftop covering at lower temperature (Figure S18B).

### Estimations of building energy savings

The building energy savings of the proposed rooftop covering are estimated as follows. On one hand, we firstly assume the heating material on the upper layer keep flat and quantify its stabilized temperature. Then, the solar absorptance and thermal emissivity of the proposed rooftop covering are identified according to the temperature of the heating material. With the optical properties given, the stabilized roof surface temperature is estimated. On the other hand, existing studies have proved that the change of roof surface temperature is highly correlated with the building energy savings, and the relationship can be quantified using linear regression model.<sup>24,61</sup> Thus, building energy simulations using EnergyPlus are conducted to obtain the roof surface temperature and building energy use in order to quantify the regression

coefficients. At last, building energy savings of the proposed rooftop covering are obtained on basis of the estimated roof surface temperature and the regression model.

The temperature of a surface  $t_s$  (°C) with given solar absorptance and thermal emissivity at the thermal equilibrium state can be estimated according to the adiabatic approximation, assuming negligible heat exchange with the underlying structure.<sup>24,69</sup> The equation at the thermal equilibrium state as well as each term of the equation are shown as follows.

$$q_{\text{solar}} - q_{\text{thermal}} - q_{\text{convective}} = 0 \quad (\text{Equation 11})$$

$$q_{\text{convective}} = h_{\text{convective}}(t_s - t_a) \quad (\text{Equation 12})$$

where,  $q_{\text{convective}}$  is the convective heat loss.  $h_{\text{convective}}$  is the convective heat transfer coefficient. In practice, the sky temperature  $t_{\text{sky}}$  (see Equation 3) is derived from the following equations.<sup>70</sup>

$$t_{\text{sky}} = \epsilon_{\text{sky}}^{1/4} \cdot t_a \quad (\text{Equation 13})$$

$$\epsilon_{\text{sky}} = \left( 0.787 + 0.764 \cdot \ln \left( \frac{t_d + 273.15}{273.15} \right) \right) \cdot (1.0 + 0.0224 \cdot CF - 0.0035 \cdot CF^2 + 0.00028 \cdot CF^3) \quad (\text{Equation 14})$$

where,  $\epsilon_{\text{sky}}$  is the sky emissivity;  $t_d$  is the dewpoint temperature (°C),  $CF$  is the cloud cover ratio.

We define hourly heating degree  $D_{\text{heat},i} = (T_{\text{set, heating}} - T_{s,i})^+$  and cooling degree  $D_{\text{cool},i} = (T_{s,i} - T_{\text{set, cooling}})^+$ , where  $\Delta T^+ = \Delta T$  if  $\Delta T > 0$ , or 0 otherwise.  $T_{\text{set, heating}}$ ,  $T_{\text{set, cooling}}$  and  $T_{s,i}$  are the indoor heating setpoint (22°C), indoor cooling setpoint (25°C) and roof surface temperature, respectively. The annual accumulated heating degrees and cooling degrees are denoted as  $D_h$  and  $D_c$  respectively, while the building heating energy use and cooling energy use are denoted as  $E_h$  and  $E_c$ , respectively. The heating energy saving  $\Delta E_h$  and cooling energy saving  $\Delta E_c$  are highly correlated with the reductions of the accumulated heating degrees  $\Delta D_h$  and cooling degrees  $\Delta D_c$ , respectively.<sup>24,61</sup>

$$\Delta E_h = k_h \Delta D_h \quad (\text{Equation 15})$$

$$\Delta E_c = k_c \Delta D_c \quad (\text{Equation 16})$$

$$\Delta E = \Delta E_h + \Delta E_c \quad (\text{Equation 17})$$

where,  $k_h$  and  $k_c$  are the linear regression coefficients, and  $\Delta E$  is the annual energy saving.

Building energy simulations on EnergyPlus platform are conducted using the roof material with five different sets of optical properties (solar absorptance, thermal emissivity), i.e., (0.9, 0.9), (0.5, 0.9), (0.1, 0.9), (0.1, 0.5) and (0.1, 0.1). Taking the associated results of (0.9, 0.9) as baseline, four sets of  $k_h$  and  $k_c$  are quantified according to Equations 15 and 16, and their average values are adopted to estimated the cooling and heating energy savings respectively. The quantification process is conducted for the five selected cities (i.e., Harbin, Beijing, Shanghai, Kunming and Hong Kong), and the annual energy saving of each city can be obtained at last.

### Quantification of solar and thermal optical properties

The spectral solar optical properties of samples including solar reflectance ( $\rho_{\text{solar}, \lambda}$ ) and transmittance ( $\tau_{\text{solar}, \lambda}$ ) were firstly measured using a spectrometer (Shimadzu UV-2450 & IR-21) with an integrating sphere. Then the total solar reflectance  $R_{\text{solar}}$  and transmittance  $T_{\text{solar}}$  are obtained by integrating  $\rho_{\text{solar}, \lambda}$  and  $\tau_{\text{solar}, \lambda}$  within the solar spectrum (Equations 18 and 19). The total solar absorptance ( $A_{\text{solar}}$ ) was calculated according to the energy balance law  $A_{\text{solar}} = 100\% - R_{\text{solar}} - T_{\text{solar}}$ . The spectral thermal optical properties of samples including thermal reflectance ( $\rho_{\text{thermal}, \lambda}$ ) and transmittance ( $\tau_{\text{thermal}, \lambda}$ ) were measured using a Fourier transform infrared (FTIR) spectrometer (PerkinElmer Spectrum 100, 2.5–15  $\mu\text{m}$ ) with a gold integrating sphere. Then the total thermal reflectance  $R_{\text{thermal}}$  and transmittance  $T_{\text{thermal}}$  are obtained by integrating  $\rho_{\text{thermal}, \lambda}$  and  $\tau_{\text{thermal}, \lambda}$  within the infrared thermal spectrum (Equations 20 and 21). The total thermal emissivity ( $\epsilon$ ) of the sample was calculated according to the Kirchhoff's law of thermal radiation  $\epsilon = 100\% - R_{\text{thermal}} - T_{\text{thermal}}$ .<sup>71</sup>

$$R_{solar} = \frac{\int_{0.3\mu m}^{2.5\mu m} \rho_{solar,\lambda} I_{solar,\lambda} d\lambda}{\int_{0.3\mu m}^{2.5\mu m} I_{0\lambda} d\lambda} \times 100\% \quad (\text{Equation 18})$$

$$T_{solar} = \frac{\int_{0.3\mu m}^{2.5\mu m} \tau_{solar,\lambda} I_{solar,\lambda} d\lambda}{\int_{0.3\mu m}^{2.5\mu m} I_{0\lambda} d\lambda} \times 100\% \quad (\text{Equation 19})$$

$$R_{thermal} = \frac{\int_{2.5\mu m}^{15\mu m} \rho_{thermal,\lambda} E_{bla,\lambda} d\lambda}{\int_{2.5\mu m}^{15\mu m} E_{bla,\lambda} d\lambda} \times 100\% \quad (\text{Equation 20})$$

$$T_{thermal} = \frac{\int_{2.5\mu m}^{15\mu m} \tau_{thermal,\lambda} E_{bla,\lambda} d\lambda}{\int_{2.5\mu m}^{15\mu m} E_{bla,\lambda} d\lambda} \times 100\% \quad (\text{Equation 21})$$

where,  $I_{solar, \lambda}$  and  $E_{bla, \lambda}$  are the spectral solar intensity (AM1.5G) and spectral blackbody radiative power at 300 K.

The solar absorptance modulation and thermal emissivity modulation were quantified by calculating the absolute difference of the optical properties at the high temperature and low temperature.

#### ADDITIONAL RESOURCES

There are no additional resources to be reported.